BAMS Article

Measuring Coupled Fire–Atmosphere Dynamics

The California Fire Dynamics Experiment (CalFiDE)

Brian J. Carroll, W. Alan Brewer, Edward Strobach, Neil Lareau, Steven S. Brown, M. Miguel Valero, Adam Kochanski, Craig B. Clements, Ralph Kahn, Katherine T. Junghenn Noyes, Amanda Makowiecki, Maxwell W. Holloway, Michael Zucker, Kathleen Clough, Jack Drucker, Kristen Zuraski, Jeff Peischl, Brandi McCarty, Richard Marchbanks, Scott Sandberg, Sunil Baidar, Yelena L. Pichugina, Robert M. Banta, Siyuan Wang, Andrew Klofas, Braeden Winters, and Tyler Salas

KEYWORDS:
Ozone;
Forest fires;
Wildfires;
Aircraft observations;
Lidars/Lidar observations;
Field experiments

ABSTRACT: The social, economic, and ecological impacts of wildfires are increasing over much of the United States and globally, partially due to changing climate and build-up of fuels from past forest management practices. This creates a need to improve coupled fire–atmosphere forecast models. However, model performance is difficult to evaluate due to scarcity of observations for many key fire–atmosphere interactions, including updrafts and plume injection height, plume entrainment processes, fire intensity and rate-of-spread, and plume chemistry. Intensive observations of such fire–atmosphere interactions during active wildfires are rare due to the logistical challenges and scales involved. The California Fire Dynamics Experiment (CalFiDE) was designed to address these observational needs, using Doppler lidar, high-resolution multispectral imaging, and in situ air quality instruments on a NOAA Twin Otter research aircraft, and Doppler lidars, radar, and other instrumentation on multiple ground-based mobile platforms. Five wildfires were studied across northern California and southern Oregon over 16 flight days from 28 August to 25 September 2022, including a breadth of fire stages from large blow-up days to smoldering air quality observations. Missions were designed to optimize the observation of the spatial structure and temporal evolution of each fire from early afternoon until sunset during multiple consecutive days. The coordination of the mobile platforms enabled four-dimensional sampling strategies during CalFiDE that will improve understanding of fire–atmosphere dynamics, aiding in model development and prediction capability. Satellite observations contributed aerosol measurements and regional context. This article summarizes the scientific objectives, platforms and instruments deployed, coordinated sampling strategies, and presents first results.

https://doi.org/10.1175/BAMS-D-23-0012.1
Corresponding author: Brian J. Carroll, brian.carroll@noaa.gov
Supplemental material: https://doi.org/10.1175/BAMS-D-23-0012.2
In final form 6 December 2023

AFFILIATIONS: Carroll, Strobach, Makowiecki, Holloway, Zucker, Zuraski, Peischl, McCarty, Marchbanks, Baidar, Pichugina, Banta, and Wang—Cooperative Institute for Research in Environmental Sciences, University of Colorado Boulder, and Chemical Sciences Laboratory, National Oceanic and Atmospheric Administration, Boulder, Colorado; **Brewer and Sandberg**—Chemical Sciences Laboratory, National Oceanic and Atmospheric Administration, Boulder, Colorado; **Lareau, Winters, and Salas**—University of Nevada Reno, Reno, Nevada; **Brown**—Chemical Sciences Laboratory, National Oceanic and Atmospheric Administration, and Department of Chemistry, University of Colorado Boulder, Boulder, Colorado; **Valero**—Wildfire Interdisciplinary Research Center, San José State University, San Jose, California, and Universitat Politècnica de Catalunya, Barcelona, Catalunya, Spain; **Kochanski, Clements, Clough, Drucker, and Klofas**—Wildfire Interdisciplinary Research Center, San José State University, San Jose, California; **Kahn* and Junghenn Noyes**—Earth Science Division, NASA Goddard Space Flight Center, Greenbelt, Maryland
*** CURRENT AFFILIATION:** Laboratory for Atmospheric and Space Physics, University of Colorado Boulder, Boulder, Colorado

Wildfires are deeply impactful events with a broad range of social, economic, and environmental consequences. Fires and emitted smoke pose major threats to health and property near populated areas and often have adverse air quality impacts with local and long-range smoke transport (Brey and Fischer 2016; Burke et al. 2021). Extreme wildfires also produce major disruptions to ecology and natural resources (Curtis et al. 2018), while lower-intensity fires help maintain ecosystem balance (Pausas and Keeley 2019). The annual economic impact of wildfires is estimated to be hundreds of billions of U.S. dollars, with one study finding an impact of $150 billion for 2018 California fires alone (Fann et al. 2018; Wang et al. 2021). Severe fire weather conditions are becoming more common in many parts of the United States, and globally, due in part to changing climate and the build-up of fuels from past forest management practices (Jones et al. 2022). It is therefore increasingly important to have rapid and accurate wildfire prediction capabilities.

Standard operational numerical weather prediction (NWP) models currently run with resolutions that are too coarse to accurately represent wildfire behavior. For wildfire prediction, specialized high-resolution fire behavior models are used that couple to NWP models (Kochanski et al. 2015; Mandel et al. 2011). These coupled fire–atmosphere models perform well in resolving wildfire plume-top height, which can be evaluated by satellite products, but many other key variables have not been rigorously evaluated due to the lack of high-resolution observations near active landscape-scale wildfires (Prichard et al. 2019). Measurements of fire-induced winds, plume dynamics and chemistry, and how these couple to fire behavior (rate-of-spread, fire intensity, etc.) are necessary to further evaluate and develop coupled fire–atmosphere models and improve the quality of information for firefighting efforts, public policy, and public safety.

Hotspot detection, fire perimeters, and fire radiative power (FRP) are currently the most available remote sensing products useful for capturing key aspects of fire behavior, with observations from polar-orbiting and geostationary satellites and operational aircraft (Kahn 2020). However, the resolutions of orbital instrumentation (e.g., VIIRS 375 m and 12 h, and GOES 2 km and 30 s) are insufficient to resolve fire dynamics at the scales needed for comprehensive tracking and prediction. Airborne multispectral imagery with resolutions $O(10)$ m and $O(1)$ min can overcome these challenges, and is thus key to studying fire behavior (Stow et al. 2019).

Wildfire-relevant atmospheric dynamics include the modulation and generation of winds, known as fire-induced winds, e.g., updrafts, inflow, and vortical motions. The buoyant updraft core over a fire typically results in upper-level divergence and lower-level convergent inflow, and this inflow feeds back to affect fire intensity, perimeter shape, and rate-of-spread (Potter 2012b). The strength and extent of inflows have not been well characterized for landscape-scale wildfires (Lareau and Clements 2017). The velocity structure of the plume, where the plume is defined as the smoke buoyantly rising from the source and advecting along the mean wind direction, depends on fire intensity and shape but is also impacted by the static stability and wind field; for example, wind shear can affect convergence and vertical mixing along with controlling downwind transport (Potter 2012a). Various mixing processes occur along the edges of the plume as well, exchanging and diluting smoky and ambient air (Rodriguez et al. 2020; Strobach et al. 2023). Horizontal-axis plume edge vortices are one such mixing process (Clements et al. 2018).

Wildfire plumes have several important air quality and meteorological impacts. Smoke transport depends on the ambient wind field and plume injection height, which can sometimes be retrieved from satellite observations (Val Martin et al. 2018). The exact makeup of fire emissions depends on a multitude of factors including fuel type and fire intensity (Sekimoto et al. 2018), but all wildfires emit large amounts of volatile organic compounds (VOCs), nitrogen oxides (NO_x), and particulate matter (PM). The VOCs and NO_x lead to rapid and prolonged ozone formation (Robinson et al. 2021; Xu et al. 2021), contributing to ozone exceedances in populated areas across continents and influencing ozone at global scales (Bourgeois et al. 2021; Gong et al. 2017: Langford et al. 2023; Rickly et al. 2023). PM is also an air quality concern at regional and continental scales (Kalashnikov et al. 2022; Sarangi et al. 2023), especially when stagnant conditions near a fire result in dangerous concentrations, e.g., smoke-filled valleys (Childs et al. 2022). Wildfire smoke can also contribute to radiative effects by absorbing or scattering sunlight. This creates a local cooling effect at the surface that can feedback on boundary layer dynamics and fire behavior (Ding et al. 2021; Huang et al. 2023; Kochanski et al. 2019) and suppress ozone photochemistry (Buysse et al. 2019; Peng et al. 2021). Particularly intense fires can produce pyrocumulonimbus (pyroCb) that inject material into the upper atmosphere (Peterson et al. 2018, 2022). Accurate prediction of plume characteristics is thus critical for NWP and air quality forecasting.

The California Fire Dynamics Experiment (CalFiDE) was designed to make novel coordinated measurements of coupled fire–atmosphere processes using airborne and ground-based mobile platforms deployed to active wildfires. The goals of this paper are twofold: to summarize the strategic design and execution of CalFiDE to aid in the planning of future wildfire studies, and to present the initial results of these unique observations toward improving fire–atmosphere process understanding and modeling.

Mobile platforms, instrumentation, and modeling

Wildfires are common throughout California and Oregon during the fire season, historically July to October. The CalFiDE deployment period spanned 28 August–25 September 2022, and was a partnered effort by the NOAA Chemical Sciences Laboratory (CSL), San José State University (SJSU), University of Nevada Reno (UNR), and NASA Goddard Space Flight Center (GSFC). Figure 1 is a map of the CalFiDE domain with markers for each fire and pictures of the instrumented platforms.

NOAA Twin Otter. The primary platform deployed for CalFiDE, the NOAA Twin Otter aircraft N57RF (TO), was initially based in Sacramento to enable observations in central and northern California. Due to fires of interest occurring farther north, the base of operations moved to Redding later in the campaign. The 3–4-h flight endurance of the TO necessitated

multiple flights per day, often making an initial transit flight with brief fire observations before refueling nearby and spending a second flight dedicated fully to observing the fire. The TO would return to base after two to three flights. TO maximum altitude was ~4.9 km ASL, and median speed ~70 m s^{-1}.

The TO CalFiDE instrumentation is listed in Table 1. A multispectral infrared (IR) imaging system (the SJSU Wildfire Imaging System–SWIS) provided geospatially located samples of the fire brightness temperature (BT), which on the same platform with a Doppler lidar allows investigation of fire–atmosphere interactions. Imagery was acquired in the midwave (3–5 μm) and longwave (7.5–13.5 μm) infrared spectral bands with a ground sampling distance (GSD) of ~2–3 m and a swath width of ~1.3–2 km. The NOAA CSL Doppler lidar on the aircraft primarily operated in conical scan mode 15°–20° off-nadir to measure horizontal wind profiles or vertical stare mode for high-resolution measurements of vertical motions. The ability to direct the lidar measurements above or below the aircraft allowed more complete observations when plumes exceeded the TO flight altitude and on low-altitude chemistry legs. The lidar relies mainly on attenuated backscatter from aerosols for its signal, with strong sensitivity to smoke, and thus also provides a qualitative profile of smoke concentration that we will call "smoke backscatter" (Banta et al. 1992; Clements et al. 2018). Both CSL lidars deployed to CalFiDE were custom-built micro-pulsed Doppler lidar systems designed in-house for mobile measurements (Schroeder et al. 2020), which includes active pointing stabilization and compensation for platform motion. The in situ gas measurements on board the TO were used for characterizing species concentrations, from emissions in the fresh plume to downwind ozone formation. Last, visual cameras mounted on the TO exterior provided continuous contextual records of the science flights, informing fire and plume evolution outside of the field-of-view of other instrumentation.

Fig. 1. (left) Map of the CalFiDE domain with observed fire locations and Twin Otter bases of operation (black points). Gray circles are ~1-h flight time from the center. (right) CalFiDE instrument platforms, including the NOAA Twin Otter aircraft, NOAA CSL Pick-Up Based Mobile Atmospheric Sounder (PUMAS), the SJSU radar truck, and the NASA *Terra* satellite with a visualization of MISR multiple look angles.

NOAA PUMAS. The NOAA CSL Pick-Up Based Mobile Atmospheric Sounder (PUMAS) is a Doppler lidar system that operates from a pick-up truck. PUMAS has a robust, rugged design capable of measurements while underway under all expected conditions, from highways to dirt roads. The PUMAS lidar had two channels, one continuously scanning at 15° off-nadir and one pointing vertically, to simultaneously measure horizontal and vertical winds. The lidar transceiver is housed in a motion compensation cradle that actively levels against truck pitch and roll, ensuring that the vertical beam is indeed vertical to within 0.5°. Like the Doppler lidar on the TO, PUMAS had a real-time display that an operator used to make adjustments as needed and to inform operational decisions based on real-time data. PUMAS also carried an in situ temperature and wind sensor. The capability to profile 3D winds while underway is unique and enabled a large part of the coordinated

Table 1. Instruments deployed during CalFiDE.

Platform	Institution	Instrument	Products
TO aircraft	NOAA CSL	Scanning Doppler lidar	Profiles of wind, vertical motion, and attenuated aerosol backscatter intensity
	SJSU	SJSU Wildfire Imaging System (SWIS)	High-resolution longwave (7.5–13.5 μm) and midwave (3–5 μm) infrared imagery
	NOAA CSL	NO_x Cavity Ring-Down (NOxCaRD)	In situ NO, NO_2, total reactive nitrogen (NO_y), O_3
	NOAA CSL and GML	Picarro analyzer	In situ CO, CO_2, CH_4, H_2O
	NOAA CSL	jNO_2 filter radiometers	NO_2 photolysis rates
	NOAA CSL	Visible-band cameras	Zenith, nadir, starboard, and port visual records
	NOAA CSL	Ocean color radiometers	Up- and down-looking intensity at seven wavelengths from 410 to 780 nm.
	NOAA CSL	Pyrometer	Surface temperature
	NOAA CSL	Nightfox	Scanning FRP and 1.6 μm imagery
	NOAA AOC	AIMMS probe	Flight-level pressure, temperature, relative humidity, and winds
PUMAS truck	NOAA CSL	Scanning Doppler lidar	Profiles of 3D wind and attenuated aerosol backscatter intensity
		Met sensor	Air temperature and wind at 3 m (mounted atop truck)
SJSU truck	SJSU	Ka-band Scanning Polarimetric Doppler Radar (KASPR)	Polarized reflectivity and line-of-sight velocity
UNR truck	UNR	Scanning Doppler lidar (Halo Photonics)	Line-of-sight velocity and attenuated aerosol backscatter
Terra satellite	NASA GSFC	Multi-angle Imaging SpectroRadiometer (MISR)	Mapped smoke plume heights, wind vectors, age estimates, aerosol particle size, sphericity, light-absorption constraints, inferred particle type
		Moderate Resolution Imaging Spectroradiometer (MODIS)	Context imagery; 4 μm brightness temperature anomalies (fire "hotspots")

sampling strategies, providing horizontal and vertical wind profiles with about 600 and 15 m along-track resolution, respectively (dependent on vehicle speed).

SJSU and UNR ground platforms. The SJSU Wildfire Interdisciplinary Research Center (WIRC) and the UNR Department of Physics have instrumented trucks with trained student–faculty teams capable of rapid deployment to wildfires. These additional assets provided a more complete picture of fire dynamics during CalFiDE, especially the SJSU Ka-band radar observations of plume evolution and particle properties (Aydell and Clements 2021). The radar also complemented the lidar capabilities since radar is most sensitive to the thickest plume, which attenuates lidar signal. The SJSU and UNR ground teams were in the field for four days and provided planning and real-time support throughout CalFiDE.

Models. To support the CalFiDE campaign, the SJSU WIRC Modeling Team produced twice-daily 48-h forecasts for selected fires using the coupled fire–atmosphere model WRF-SFIRE (Mandel et al. 2011). Each forecast was initialized around 0800 and 2000 local time (LT; 0300 and 1500 UTC) using the 0000 and 1200 UTC NAM218 product as a source of initial and boundary conditions. Each forecast was completed, visualized, and posted online within 6–10 h. Horizontal resolutions varied from 333 to 500 m. The coupled fire–atmosphere forecasts were executed using the WRFx framework (Mandel et al. 2019), which automates data acquisition, processing, model execution, visualization, and data presentation via a dedicated web portal. WRFx was run with the fuel moisture data assimilation system, executed hourly to integrate dead fuel moisture observations from automated weather stations. IR fire perimeters, satellite fire detections, and meteorological forcing data were processed within WRFx to produce high-resolution forecasts of wind, fire spread, plume height and location, and surface and vertically integrated PM2.5.

The fire state at the beginning of each forecast was initialized by utilizing the latest IR observations and satellite fire detections. Each forecast started with a 2-h spinup phase, during which fire initiation was carried out using the gradual ignition method outlined in Kochanski et al. (2023). This initialization procedure was implemented to selectively initiate active areas of the fire, preventing model destabilization caused by sudden fire heat release. Additionally, it facilitated the spinup of pyroconvection at the onset of each forecast, improving the initial representation of the plume structure.

The forecasts, shared on the dedicated web portal, provided CalFiDE planning operations with an outlook for fire growth, plume development, and smoke dispersion. Table S1 in the online supplemental material provides additional details, including resolutions and output variables.

Novel wildfire sampling strategies

The fires. Table 2 lists descriptions of each fire, observation dates, and platforms deployed. Figure 2 shows photos taken at each fire. Platforms were deployed together when possible, but in some cases this was not feasible due to down-days or fire location; e.g., the Cedar Creek Fire was within the TO range but was too far for the ground-based teams to target. The fires ranged from the small slow-moving Red Fire to the Mosquito Fire, which was the largest fire in California in 2022, and Cedar Creek Fire, the second largest in Oregon. All occurred in complex mountainous terrain. All except the Red Fire produced pyrocumulus or pyrocumulonimbus on observed days.

Sampling strategies. CalFiDE operations were centered around the afternoon, when wildfire intensity typically peaks alongside the ambient temperature maximum and relative humidity minimum. Forecasters monitored conditions and models daily and contributed to mission planning meetings each morning. Satellite overpass timing from the MISR instrument on NASA *Terra* was also considered during planning since these measurements of particle properties and plume heights contributed to CalFiDE science.

Constant communication was essential in the rapidly changing environment of wildfires to ensure safety and coordination between mobile platforms. A group messaging program was used to disseminate plans and fire or meteorological conditions while in the field, including text, images, and files. When deployed to a fire, PUMAS and the TO were also able to communicate via radio to coordinate overpasses or plan changes, which was

Table 2. Fires observed during CalFiDE.

Incident name	State	Location (lat, lon)	Start date (2022)	100% containment date	Total burn area (acres)	CalFiDE observation dates	Area burned on observation dates (acres)	Platforms present
Red Fire	CA	37.661°,–119.471°	4 Aug	Late October	8,410	28 Aug	—	TO, PUMAS
Rum Creek Fire	OR	42.641°,–123.628°	17 Aug	Late September	21,347	30 Aug, 1 Sep	3,325	TO, PUMAS, *Terra* (30 Aug)
Mountain Fire	CA	41.459°,–122.627°	2 Sep	20 Sep	13,440	3–6 Sep	8,295	TO (3–4 Sep, 6 Sep); PUMAS (5–6 Sep); UNR and SJSU (6 Sep)
Mosquito Fire	CA	39.006°,–120.745°	6 Sep	27 Oct	76,788	7–11 Sep, 22–25 Sep	45,801	TO (7–9 Sep, 11 Sep, 22–25 Sep), PUMAS, UNR (7–8 Sep), SJSU (7–8 Sep, 10 Sep), *Terra* (8 Sep)
Cedar Creek Fire	OR	43.726°,–122.167°	1 Aug	Early November	127,311	10 Sep, 20 Sep	12,003	TO

especially valuable in areas without cell service. Each platform's unique and complementary capabilities were coordinated to capture the evolution of fire behavior, fire-induced winds and ambient conditions, and fire emissions and chemistry.

The TO flight hours were largely dedicated to flying over the fires, with the IR imagery observing fire behavior evolution while the Doppler lidar pointed nadir to measure updraft velocity, turbulent mixing, and plume structure via smoke backscatter. Passes over the fire had about a 5–20-min revisit time, typically repeating the same leg back and forth for maximum temporal resolution. Before and after each repeat vertical stare leg, the lidar was switched from nadir stare to wind profiling mode to measure the horizontal winds near the fire. Figure 3a exemplifies this scanning strategy on a blow-up day at the Mosquito Fire. On this day the plume updraft region was too deep and intense for the TO to fly far within the fire perimeter, so a safe flight path was chosen that sampled back-burns and inflow winds on the upwind side of the fire. Figure 3b exemplifies a flight pattern where the TO was able to fly above the fire throughout the fire perimeter, executing a box pattern to characterize winds before and after repeat sampling directly over and downwind of flaming areas.

Fig. 2. Photos of each fire observed during CalFiDE. (a) Red Fire, (b) Mountain Fire, (c) Rum Creek Fire from TO (top) and PUMAS (bottom), (d) Mosquito Fire, (e) Cedar Creek Fire, and (f) smoky valley from the smoldering Mosquito Fire on an air quality flight 2 weeks after the image in (d).

Both the IR imaging system and the Doppler lidar had real-time data visualization capabilities that were leveraged to adjust flight plans to the evolving fire and atmospheric conditions. TO flight paths were also continuously adjusted to avoid interfering with firefighting activities. TO pilots were in constant radio communication with air traffic controllers to successfully integrate into the restricted airspace around these fires.

PUMAS measured winds near the fires, to inform changes relevant to fire behavior and complement the fire-induced winds measured by the TO lidar. Depending on road accessibility (given complex terrain, road closures, and safety considerations), this meant either staying in one upwind location (Fig. 3a) or driving repeated legs (Fig. 3b). The driving legs provided spatially resolved winds and smoke backscatter, but legs were kept to a short revisit time (≤1 h) to minimize ambiguity between spatial and temporal variability when interpreting the data. In some cases, the scan geometry of the PUMAS lidar wind profiling (an upward-facing cone) was essential to characterizing wind low in valleys, where the downward-facing cone of the TO lidar footprint (~1–4 km across at the surface) would not be able to resolve.

The SJSU and UNR assets, when present, deployed at an appropriate range for the radar to sample the plume.

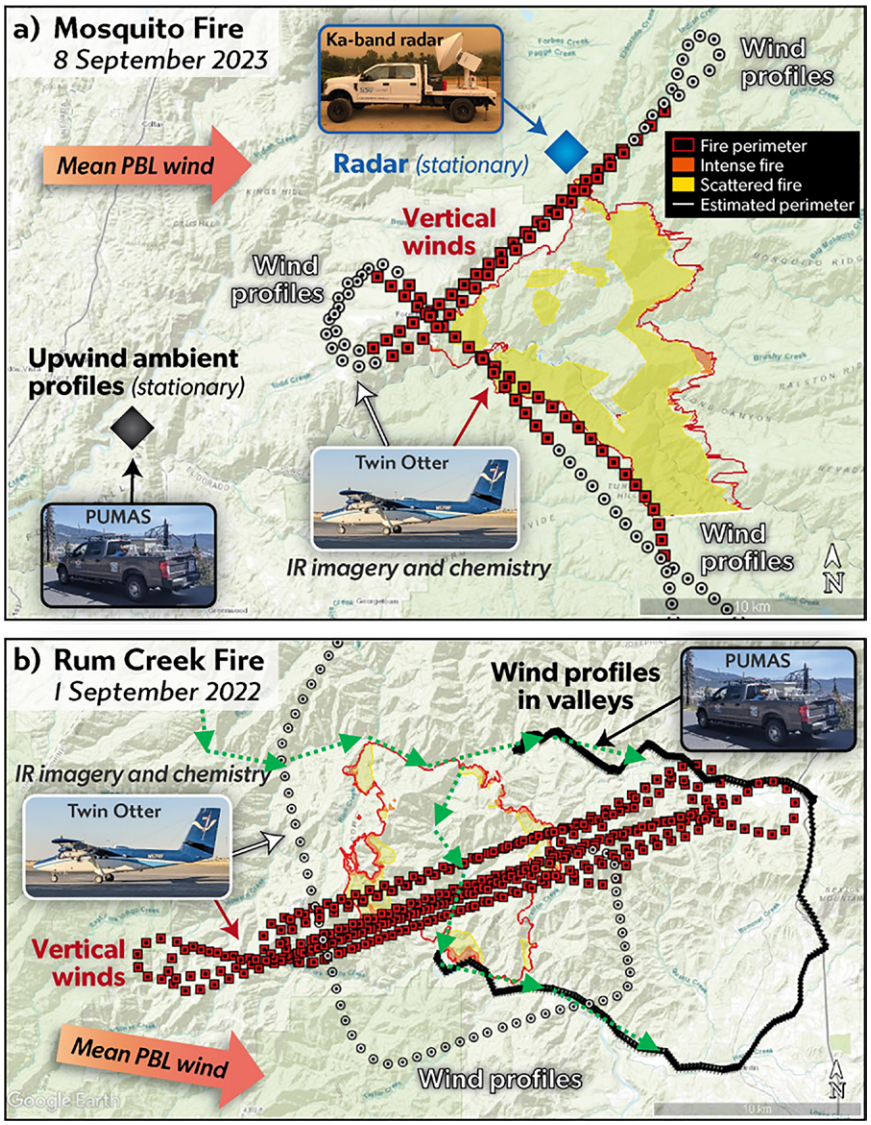

Fig. 3. Examples of mobile platform sampling strategies during CalFiDE. (a) 8 Sep Mosquito Fire perimeter in red, with yellow/orange shading indicating active fire (National Interagency Fire Center 2023). Twenty-five minutes of the TO flight track is shown with white circles (when lidar was scanning for wind profiles) and red squares (nadir stare). PUMAS (black diamond) and the UNR and SJSU platforms (blue diamond) were stationary upwind of the fire. (b) The Rum Creek Fire perimeter on 1 Sep along with the TO flight track indicating lidar mode, as in (a). The black track is a repeated PUMAS route along the valley floors. The green arrows indicate the location and direction of a sea breeze that advanced up the river valley and split into both valleys near the fire. Orange arrows in (a) and (b) indicate mean wind in the planetary boundary layer (PBL), though there was wind shear spanning the plume depth in both cases.

Initial observations and results

This section presents selected observations and preliminary analyses from the CalFiDE datasets, highlighting the synergistic instrumentation and mobile platform capabilities for sampling coupled fire–atmosphere dynamics and chemistry.

Fire behavior and winds. Figure 4 provides a geospatially contextualized visualization of the airborne and PUMAS lidar data at the Rum Creek Fire on 1 September. PUMAS simultaneously provided profiles of winds and smoke backscatter throughout the complex terrain. On this day stagnant conditions (<2 m s^{-1}) persisted in the valleys until around 1400 LT, allowing accumulation of a dense smoke layer confined below 1 km (Fig. 4a, top right). A sea breeze advanced up the river valley in the late afternoon (green arrows in Fig. 3b), bringing stronger winds and cleaner air, with a terrain-following but roughly northwesterly wind

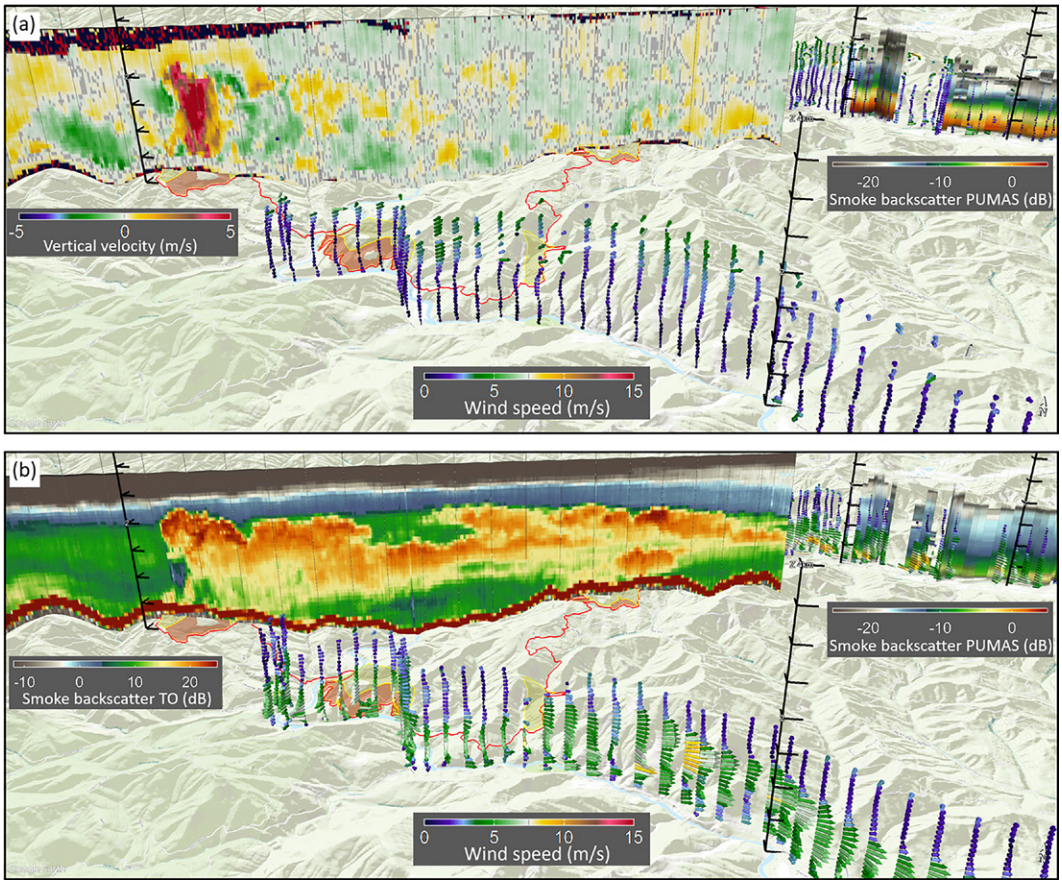

Fig. 4. Airborne and truck-based mobile Doppler lidar observations at the Rum Creek Fire on 1 Sep, along the same tracks shown in Fig. 3b. Arrows scale length and color with wind speed from PUMAS. The red line is the fire perimeter, with yellow/red shading for more active areas of the fire (National Interagency Fire Center 2023). Black axes have 500 m vertical increments. (a) PUMAS observations from ~1330 LT, with stagnant conditions in valleys. Smoke backscatter panels in the top-right corners indicate a thick smoke layer confined near the surface. (b) PUMAS observations from ~1800 LT, when a sea breeze had strengthened in the valleys and the shallow smoke layer is far less severe. The curtains in the top left of (a) and (b) are from the airborne lidar at 1637 LT, showing vertical velocity in (a) and corresponding smoke backscatter in (b).

direction and a maximum depth of about 1 km above the valley floor. Winds above the valleys were of a distinctly different regime throughout the day, with southerly winds ~6–8 m s^{-1} at the top of the fire plume and weaker backing winds in the shear layer between the aloft and valley conditions. The unique capability of the mobile lidars to measure these evolving winds in and above the valleys and throughout the area is important, as the smoke transport is subject to these conditions based on injection height and time.

At the same time as the PUMAS measurements, the TO flew repeated legs over the fire while staring downward (Figs. 3b and 4). These legs were oriented along a southwest–northeast line to follow the plume downwind, aligning with the southwesterly wind direction in the shear layer noted in the previous paragraph. The vertical velocity profiles over the fire have been used to identify a Gaussian shape to the updraft core and an approximately linear increase of updraft strength with height, until reaching a capping inversion (not shown in detail here). Some overturning or vortical motions are also captured in Fig. 4a, evidenced by velocity couplets near the updraft core. Downwind, the strength of vertical motions diminishes and the largest plume (leftmost in Fig. 4b) narrows vertically, and additional smoke is injected at lower levels from lower-intensity burning on the right side of the fire perimeter as well as aloft from other areas of the fire. The spatiotemporal structure and scales of motion of these plumes can be analyzed, coupled with the evolving IR fire intensity over repeated legs.

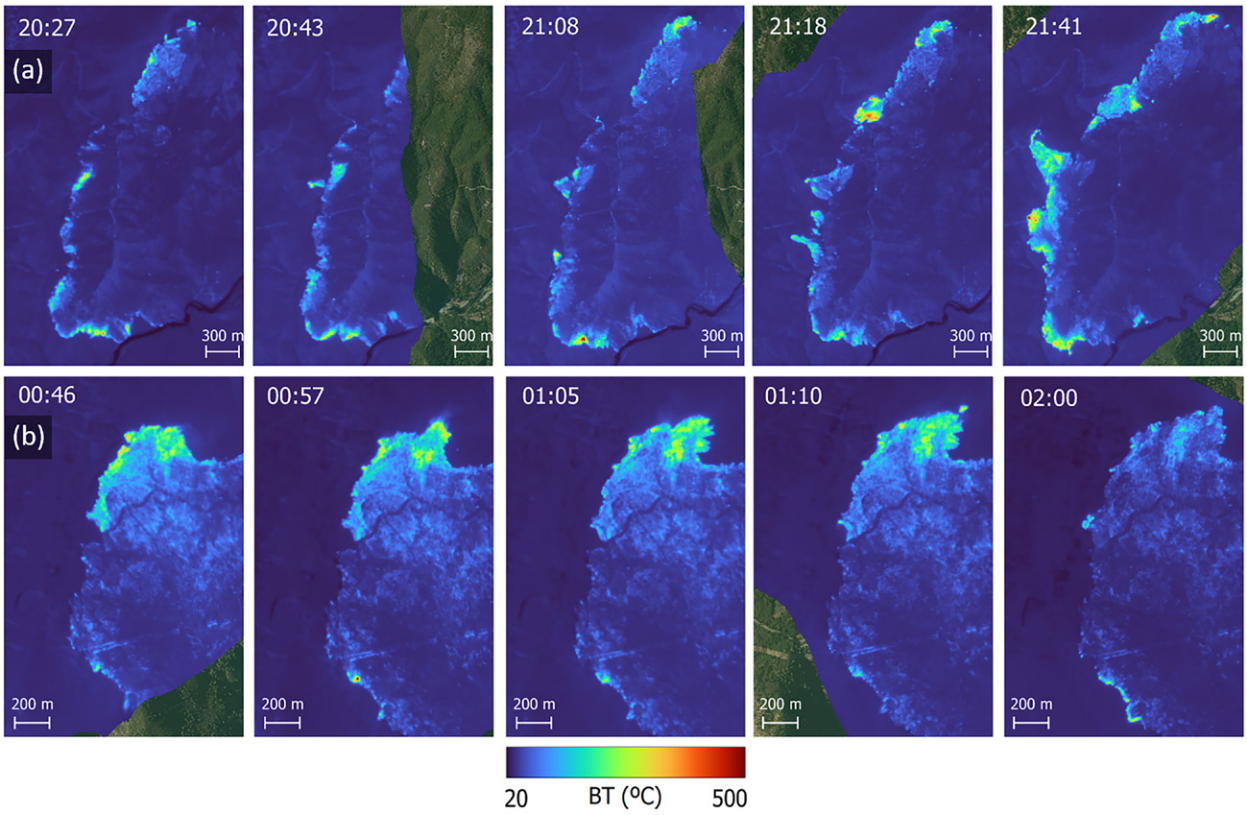

Fig. 5. Example of high-resolution fire progression observations made on the west side of the Mosquito Fire using airborne longwave IR imaging on 8 Sep in (a) the early afternoon and (b) the evening. Times are UTC, and sunset was at 0222 UTC. BT values are estimated from sensor irradiance with no atmospheric corrections. Base imagery provided by the USDA National Agriculture Imagery Program (U.S. Geological Survey 2016).

Figure 5 shows an example of the fire behavior observations acquired by SWIS during CalFiDE, with observations of the Mosquito fire western edge at different times on 8 September as the fire progressed toward the communities of Foresthill and Volcanoville. Short flight revisit times and the spatially resolved radiometric measurements allow the analysis of fire dynamics with high spatial and temporal resolution, including spotting (Fig. 5b, top right of 0110 UTC image) and finger-like spread (Fig. 5a).

Figure 6 is again from 8 September at the Mosquito Fire. Figure 6a shows IR imagery of the remnants of a burn that had progressed upslope toward the town of Volcanoville, which occupies the lower half of Fig. 6a outside of the burn area. Figure 6b combines the imagery with coincident lidar data. The lidar wind profile informs ambient inflow at low levels and winds impacting plume motions aloft, while the smoke backscatter details plume structure that is explored further in Fig. 7. Considering the wind direction, the plume captured by the lidar was likely generated at the highest observed BTs along the fire front in the lower-left quadrant of Fig. 6a.

Figure 7 further explores the plume shown in Fig. 6b. This case occurred within 30 min of sunset when convective daytime turbulence had already subsided, as evidenced by the lack of strong turbulent eddies outside of the plume. The TO passed over a hotspot at 0203 UTC (Fig. 7a) that consisted of an updraft core tilted along the mean wind direction, flanked by edge vortices evidenced by the adjoining negative velocities in two mushroom-shaped billows. Each of the four largest vortices spans ~500 m altitude. Fourteen minutes later, another overpass (Fig. 7b) shows the updraft core deepened and broadened and was followed by plume undulations downwind, likely resulting from vortices advected downwind and modified by background stratification. The maximum updraft velocity observed in both overpasses

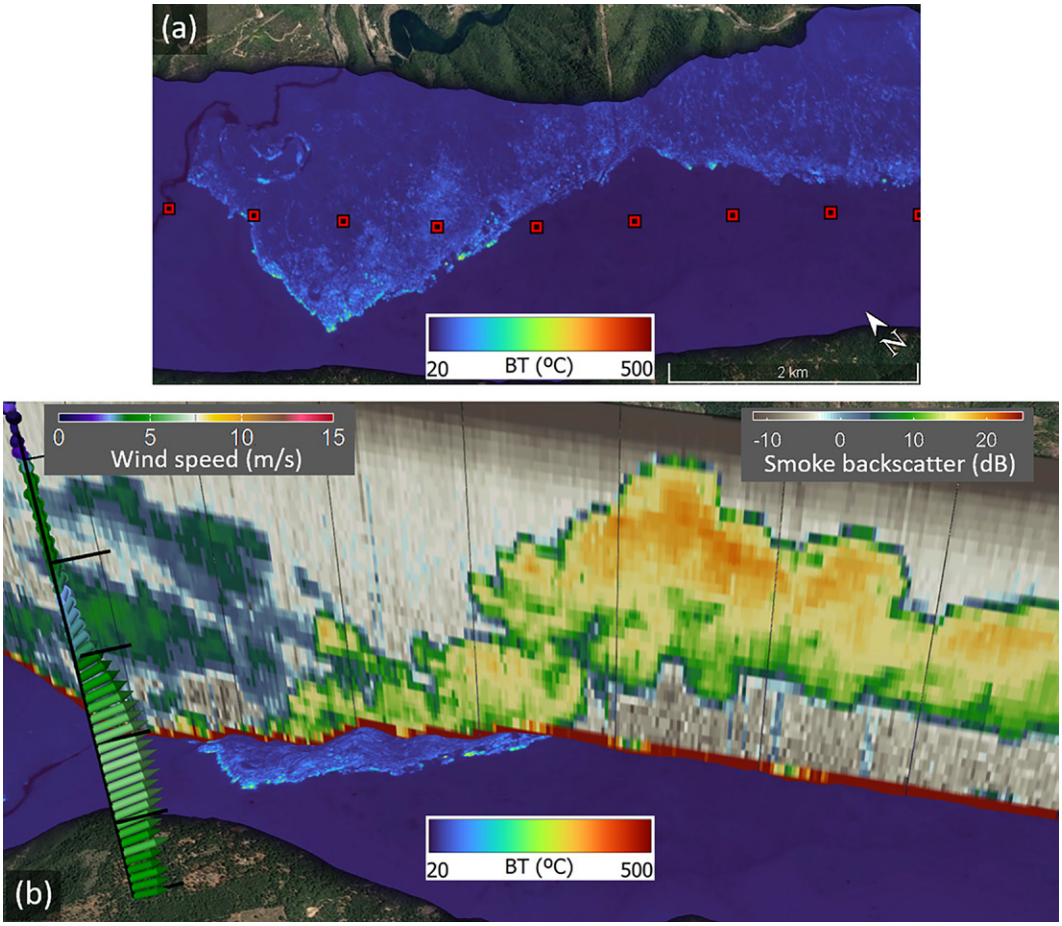

Fig. 6. The southwest edge of the Mosquito Fire at 0217 UTC 9 Sep. Combined visualization of airborne longwave IR BT as in Fig. 5 with (a) the TO flight track (red squares at 10-s intervals) viewed from above and (b) airborne Doppler lidar horizontal wind profile (arrows) and smoke backscatter (curtain) viewed from an angle. The smoke backscatter data are from a vertical stare leg detailed further in Fig. 7, while the wind profile was retrieved using scanning data from both ends of the vertical stare leg to represent the mean ambient wind. Note the figure perspective is tilted in (b) relative to (a). Black lines along the wind profile are a vertical axis with 500 m increments.

was ~6 m s^{-1}. There was weak wind speed shear across the plume depth but very little directional shear. The largest IR BTs were near the base of the plume.

More quantitative analysis coupling fire evolution from the IR data to updraft strength and other dynamics is still to come, spanning four overpasses from this case and dozens more throughout the campaign. Unprecedented capabilities of these lidar observations include the isolation of the vertical velocity by flying directly over the fire, and the along-track extent following the plume kilometers downwind, informing plume rise and mixing processes across scales O(100–1,000) m.

Fire emissions and chemistry.

Figure 8 illustrates the synergy of chemistry and lidar observations from multiple flight legs downwind of the Mosquito Fire: the first leg flew through the top of the plume, the second leg just above it, and the third and fourth within the plume at two different altitudes. Real-time lidar data provided smoke backscatter profiles to identify altitudes for the subsequent chemistry legs. Variable mixing ratios of NO_x, NO_y, ozone, and CO during smoke penetration legs resulted from differences in emissions, plume age, and degree of photochemical processing. The photochemical processing was also affected in part by aerosol shading by the overlying smoke layers, as measured by NO_2 photolysis rates (e.g., Fig. 8e). The NO_x and NO_y mixing

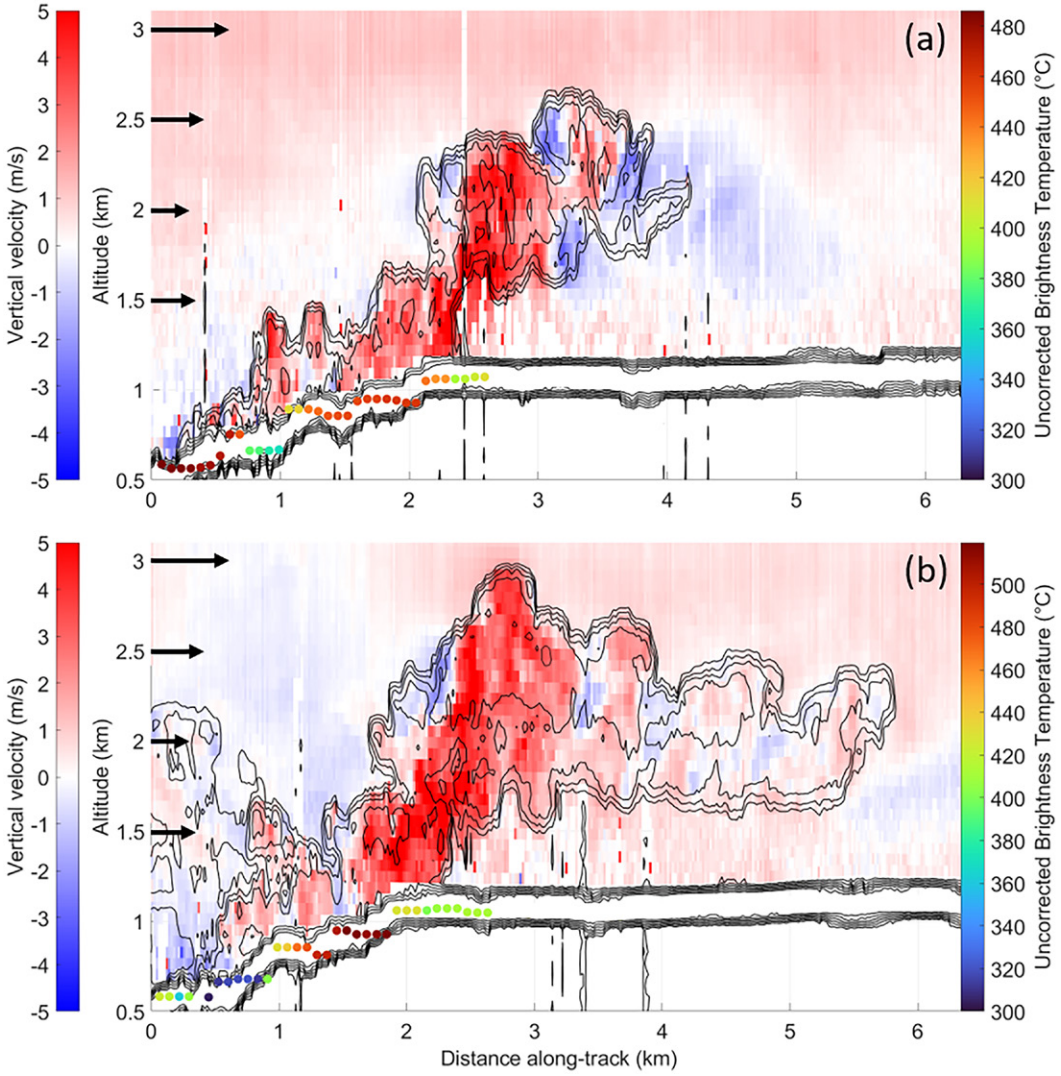

Fig. 7. Mosquito Fire airborne lidar measurements for the flight leg shown in Fig. 6a. The Doppler lidar vertical velocity is plotted on the red-blue color scale, overlaid with thin black contours of smoke backscatter indicating the plume at (a) 0203 and (b) 0217 UTC along the same transect. Black arrows indicate mean in-plane wind speed, scaled relatively to show vertical shear. Longwave IR BT is plotted at the surface for a qualitative indicator of fire intensity, taken as the max BT from the entire camera field of view (and bounded by backscatter contours due to the strong signal return from the surface).

ratios were enhanced above background levels on all plume transects in this example, with evidence for large NO_x emissions and ozone mixing ratios up to 120 ppb.

Figures 8f–h show several metrics for emissions and photochemistry, using the first plume transect from Fig. 8a as an example. Figure 8f shows NO_y versus CO, where NO_y is an approximately conserved quantity and a measure of the amount of NO_x at emission. The normalized excess mixing ratio (NEMR) (Yokelson et al. 2013) of 15.3 ppb ppm^{-1} from the correlation plot indicates a high NO_x/CO ratio, consistent with a hot, flaming stage fire (Roberts et al. 2020). The middle plot shows NO_x/NO_y, a measure of plume age or the degree of photochemical aging; in this case approximately half of the emitted NO_x had been oxidized. Finally, the ratio of O_3 to $NO_z = (NO_y - NO_x)$ in the right plot is the ozone production efficiency (OPE), or the amount of ozone produced per unit NO_x emitted and oxidized (Trainer et al. 1993). This metric can alternately be plotted as odd oxygen, $O_x = O_3 + NO_2$, against NO_z, where O_x is a more conserved quantity than O_3. These three plots are just one example of a single plume intercept, but there are many such intercepts across the CalFiDE dataset sampling a range of fire conditions that will provide statistics on the variability in NO_x emissions and ozone photochemistry from wildfires.

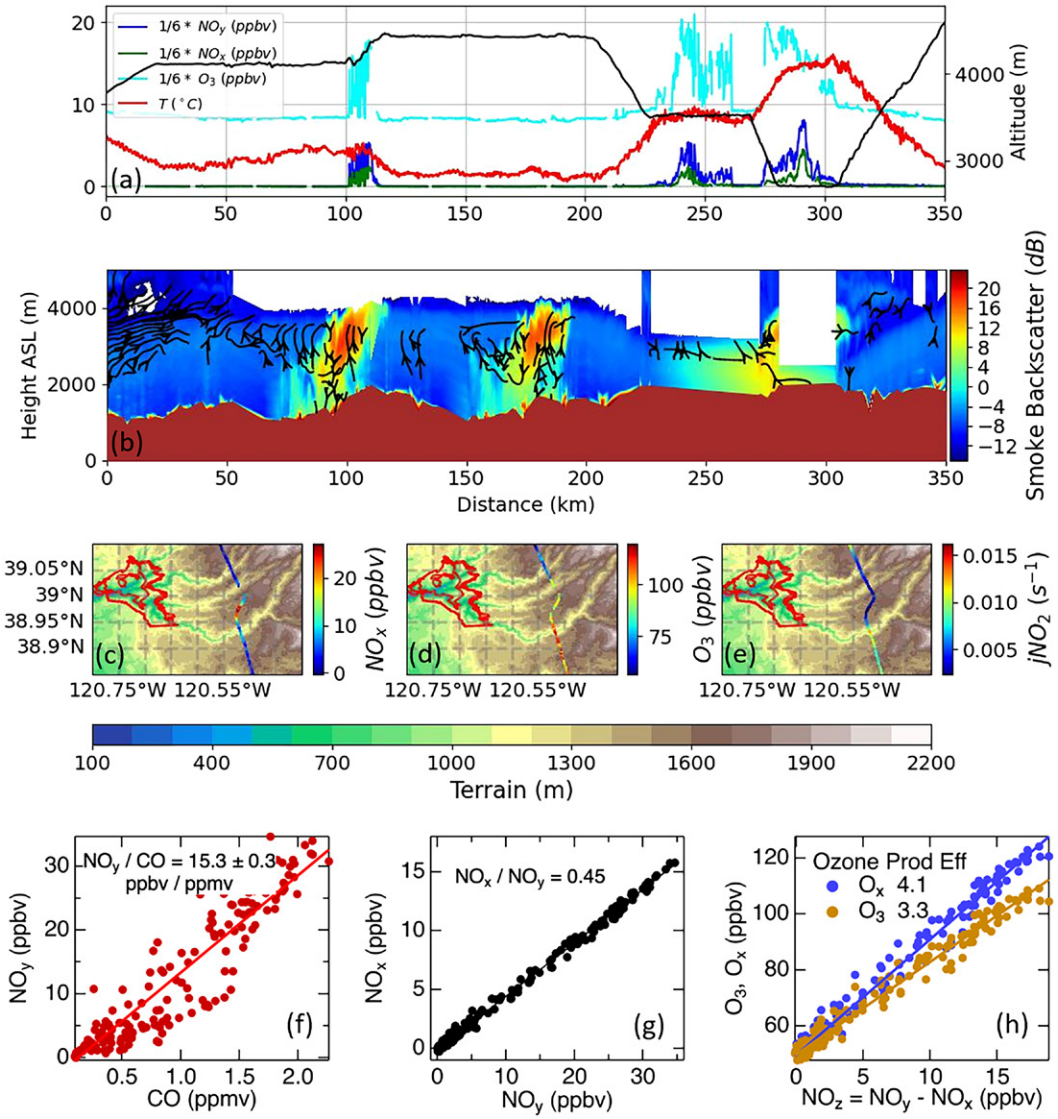

Fig. 8. (a) TO altitude, air temperature, and scaled NO_y, NO_x, and ozone at flight level. (b) Lidar RCI with overlaid streamlines derived from combining horizontal and vertical wind measurements (vertical motions are magnified for visibility). White gaps in the data are above the aircraft when the lidar was only pointing downward (i.e., not alternating scans up and down). (c)–(e) Flight level NO_x, ozone, and NO_2 photolysis rate for one downwind flight leg, with the fire perimeter in red (National Interagency Fire Center 2023). (f)–(h) Scatterplots of NO_y:CO, NO_x:NO_y, and O_x:NO_z highlighting emissions, plume age, and ozone production efficiency, respectively, from the first transect in (a). The use of color in (f)–(h) is solely to visually differentiate the data.

Small temperature increases (<2°C) were also observed in the plumes at around 105 and 245 km and above the plume at around 180 km in Figs. 8a and 8b. This suggests that the plume was still buoyant and offers some insight to the left-over kinetic energy of the buoyantly driven plume at these levels. Outside the plumes, the lidar wind retrievals were relatively limited due to a lack of aerosol, but show circulation patterns on the edges that may be transporting smoke down and away from the main plume (clockwise, on the left edge of the first two legs).

Radar and satellite plume characterization. NASA's *Terra* satellite overflew the Mosquito Fire plume on the morning of 8 September, enabling retrieval of plume properties using the MISR instrument. Figure 9a shows the plume at 1849 UTC imaged by MISR, with hotspots from MODIS superposed. Plume heights (Fig. 9b) and the associated motion vectors were derived geometrically, at 1.1 km horizontal resolution and between 250 and 500 m vertical

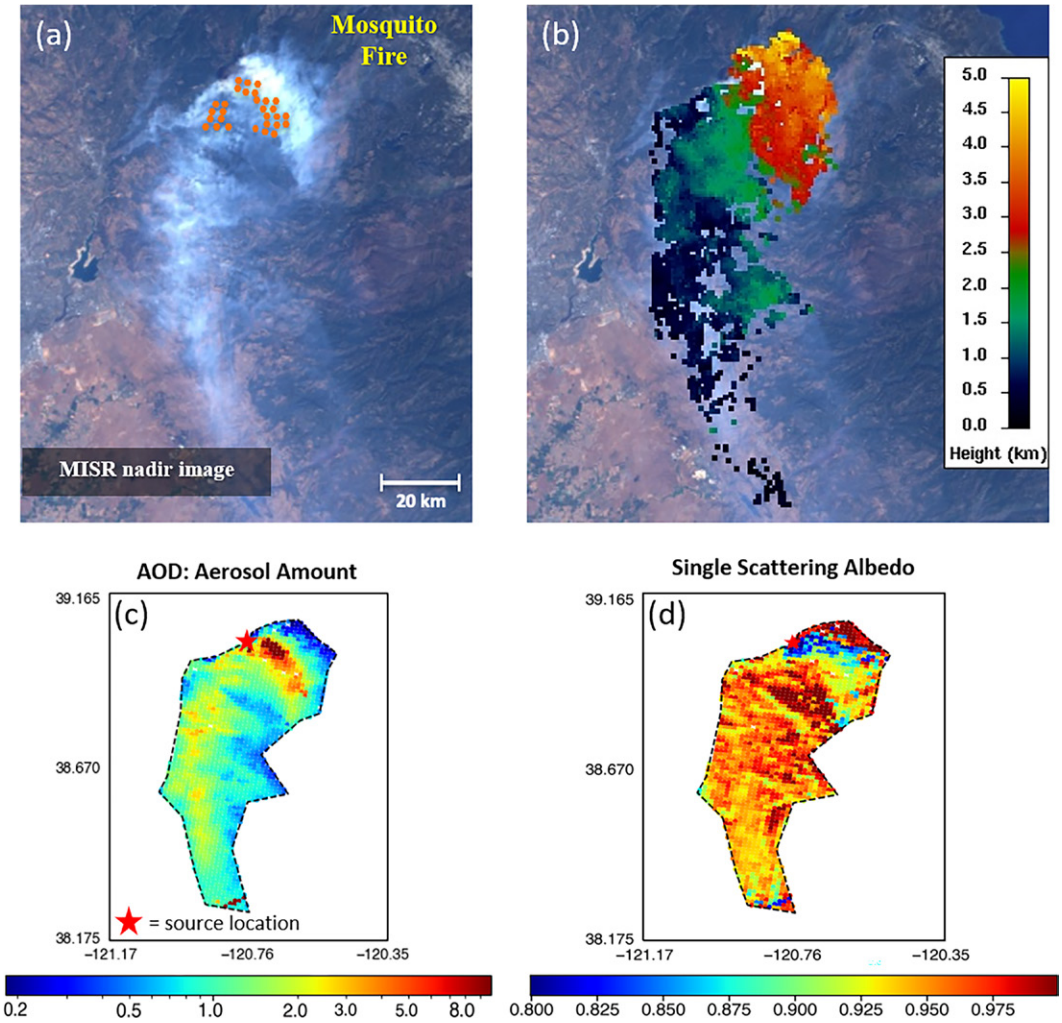

Fig. 9. (a) MISR nadir RGB image of the Mosquito Fire plume at 1849 UTC 8 Sep, with MODIS 4 μm thermal anomalies (orange dots) superposed, (b) MISR wind-corrected plume-top height map, (c) mid-visible AOD, and (d) aerosol single-scattering albedo retrieved at 1.1 km horizontal resolution from the MISR research aerosol retrieval algorithm. (Adapted from Junghenn Noyes and Kahn 2023.)

resolution, from MISR stereo imagery. Aerosol optical depth (Fig. 9c) and particle light absorption (Fig. 9d), size, and sphericity constraints were retrieved radiometrically. Plume age, black smoke, and brown smoke were also inferred from the MISR data. This dataset is presented in detail in Junghenn Noyes and Kahn (2023).

The fire intensified after the MISR overpass, and the SJSU Ka-band radar captured the structure and polarimetric properties of the deeper pyroCb-topped plume in the afternoon, summarized in Fig. 10. Figure 10a shows the plume structure constructed with reflectivity from multiple RHI (constant azimuth angle, variable elevation) and PPI (constant elevation angle, variable azimuth) scans. This indicates an updraft column rising from the active regions of the fire, a broadening plume within the pyroCb aloft, plume tops above 12 km MSL, a detraining anvil region, and possible ash fallout. MISR and the SJSU radar did not observe at the same times, so the measured plume-top heights cannot be directly compared. However, the two platforms do provide insight to the plume-top growth from 5 to 12 km over ~3.25 h.

The microphysical and kinematic structures of the pyroCb-topped plume are elucidated by examining data from two RHI slices, the scan-planes of which are contextualized with NEXRAD radar echo tops (Fig. 10b) and *GOES-17* visible satellite data (Fig. 10c). The first RHI slice was through the windward plume edge (Figs. 10d–f), capturing two updraft cores and a thin anvil spreading toward the radar from the overshooting pyroCb.

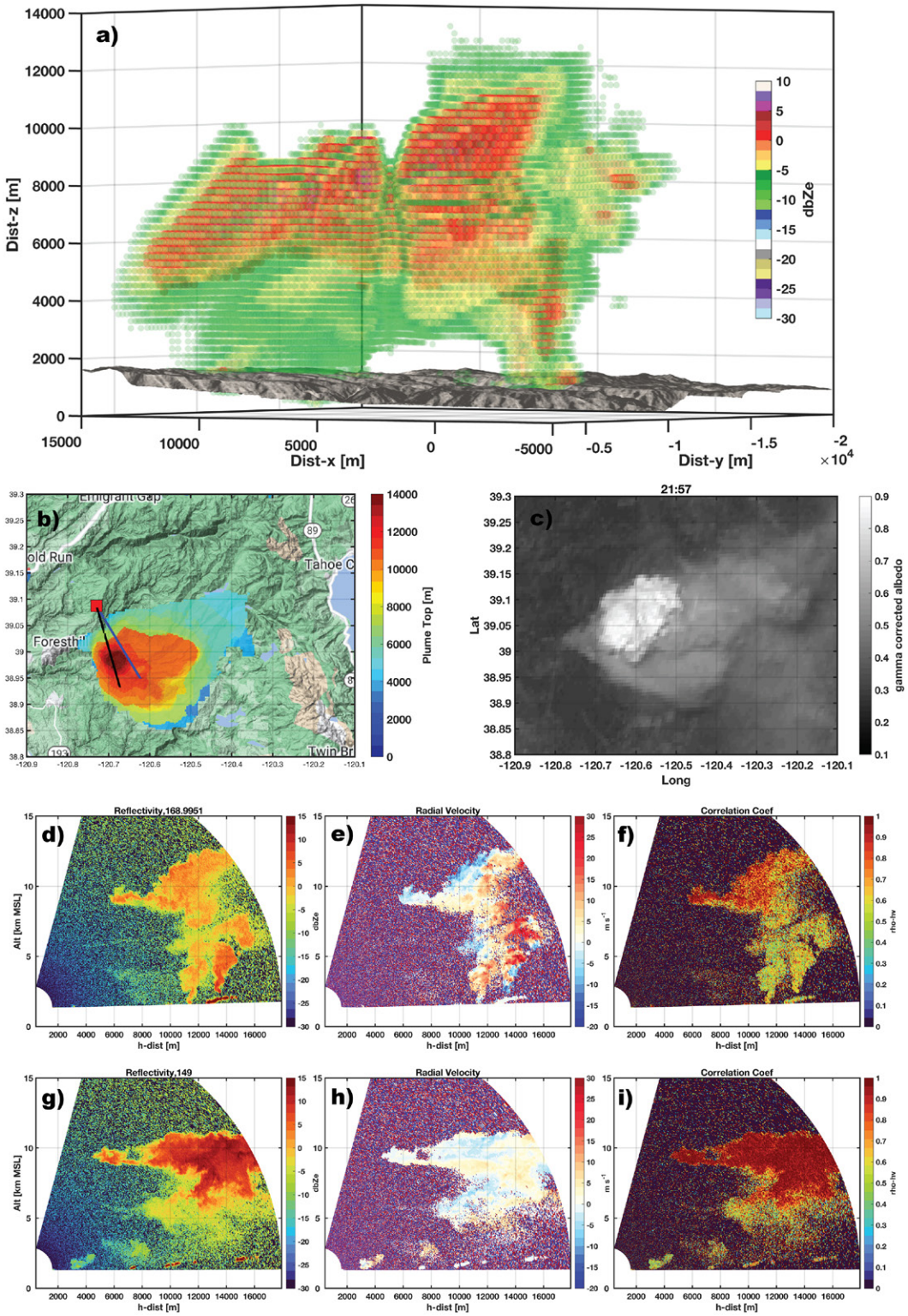

Fig. 10. Ka-band pyroCb-topped plume observations during the Mosquito Fire at ~2200 UTC 8 Sep. (a) 3D reconstruction of the plume using semitransparent dots with colors corresponding to reflectivity. (b) NEXRAD echo-top heights and selected radar scan planes. (c) *GOES-17* visible imagery matching (b), but note GOES has a parallax offset (tall components projected farther north). The scans shown in (b) are summarized in (d)–(f) (black line) and (g)–(i) (blue line) with (d),(g) reflectivity, (e),(h) radial velocity, and (f),(i) correlation coefficient.

The highest reflectivity was in the plume base, due to pyrometeor loading. The kinematic structure shows strong horizontal and vertical motions, with maximum outbound flows of ~30 m s^{-1}. Notably, the correlation coefficients (Fig. 10f) were low near the plume base and greater in the upper plume, indicating that quasi-spherical hydrometeors provide the

primary radar scatter aloft whereas oblate pyrometeors are dominant through the lower 2/3 of the plume.

For contrast, Figs. 10g–i shows a scan further downwind. This scan sliced through the pyroCb's spreading anvil as it advected away from the updraft core, subsided, and broadened. Notably the reflectivity values were larger than in the updraft, and the correlation coefficient indicates the returns were dominated by hydrometeors. This suggests that the hydrometeors grew downwind from the updraft, and the structure of the reflectivity suggests some virga was falling from the plume. This is a potentially important process in that it can cause downdrafts from the pyroCb.

These data indicate the enormous potential for scanning polarimetric radars to provide new insights into deep convective plumes and pyroCb processes, as well as the capability of satellite observations to supplement field measurements with additional plume properties. Ongoing efforts will couple these observations to fire behavior, dynamics, and chemistry, where possible, using the other CalFiDE observations.

Summary and future work

To counter the increasing threat from wildfires to health, economy, and ecology, accurate coupled fire–atmosphere forecast models are needed. Validating these models is difficult due to the scarcity of observations near active wildfires. CalFiDE was designed to make such challenging observations using airborne and ground-based mobile platforms to measure coupled fire–atmosphere processes. This article detailed capabilities and coordinated sampling strategies from CalFiDE, including novel measurements of fire-induced winds coincident with IR fire mapping. Observations included spatial and temporal sampling of

1) updraft speed, vortical mixing, and inflow at $O(10–1{,}000)$ m;
2) plume structure and motions from source to injection height to several kilometers downwind;
3) fire location, rate-of-spread, and radiative power at $O(1)$ m and $O(10)$ min;
4) fire emissions and ozone chemistry in fresh plumes and up to days after emission;
5) stagnant smoke-filled valleys progressing to cleaner air;
6) satellite retrievals of plume height and aerosol properties;
7) polarimetric radar plume characterization of a pyroCb.

CalFiDE also demonstrated the utility of a single small aircraft with a limited but diverse payload to serve a breadth of science goals, especially when supported by other assets, as well as the feasibility of collecting scientific measurements without interfering with fire management operations. The successful coordination between multiple research teams and emergency responders during CalFiDE demonstrates the benefits that emerge from multidisciplinary and multisectoral collaboration.

Combining these mobile multidimensional datasets for analysis is a complex and new challenge that must be executed carefully. Thus, many of the conclusions and new findings from CalFiDE are yet to come and will arise from ongoing efforts, including evaluation of fire–atmosphere and air quality models. Presenting the logistics, execution, and first results from CalFiDE will also hopefully promote similar research efforts in the future.

Acknowledgments. We thank the many participants who helped make CalFiDE a success, especially the TO pilots and NOAA AOC. The TO and PUMAS were supported in part by NOAA Cooperative Agreements NA17OAR4320101 and NA22OAR4320151, as well as Public Law 117-43 Disaster Relief Supplemental Appropriations Act signed 30 September 2021 including $55M (ORF) related to the consequences of hurricanes and wildfires in calendar years 2020 and 2021. The SWIS IR

imaging system deployment was supported by NSF Award 2053619. R. A. Kahn was supported in part by the NASA Atmospheric Chemistry Modeling and Analysis Program (ACMAP), and K. T. J. Noyes by ACMAP and the NASA Postdoctoral Program. Thanks to Chelsea Thompson for assistance with Figs. 1–3. The statements, findings, conclusions, and recommendations are those of the authors and do not necessarily reflect the views of NOAA or the U.S. Department of Commerce.

Data availability statement. Data from CalFiDE are archived on the NOAA CSL web page: https://csl.noaa.gov/groups/csl7/measurements/2022calfide/.

References

Aydell, T., and C. B. Clements, 2021: Dual-polarimetric Ka-band Doppler radar observations of wildfire plumes. *Mon. Wea. Rev.*, **149**, 1247–1264, https://doi.org/10.1175/MWR-D-20-0198.1.

Banta, R. M., L. D. Olivier, E. T. Holloway, R. A. Kropfli, B. W. Bartram, R. E. Cupp, and M. J. Post, 1992: Smoke-column observations from two forest fires using Doppler lidar and Doppler radar. *J. Appl. Meteor.*, **31**, 1328–1349, https://doi.org/10.1175/1520-0450(1992)031<1328:SCOFTF>2.0.CO;2.

Bourgeois, I., and Coauthors, 2021: Large contribution of biomass burning emissions to ozone throughout the global remote troposphere. *Proc. Natl. Acad. Sci. USA*, **118**, e2109628118, https://doi.org/10.1073/pnas.2109628118.

Brey, S. J., and E. V. Fischer, 2016: Smoke in the city: How often and where does smoke impact summertime ozone in the United States? *Environ. Sci. Technol.*, **50**, 1288–1294, https://doi.org/10.1021/acs.est.5b05218.

Burke, M., A. Driscoll, S. Heft-Neal, J. Xue, J. Burney, and M. Wara, 2021: The changing risk and burden of wildfire in the United States. *Proc. Natl. Acad. Sci. USA*, **118**, e2011048118, https://doi.org/10.1073/pnas.2011048118.

Buysse, C. E., A. Kaulfus, U. Nair, and D. A. Jaffe, 2019: Relationships between particulate matter, ozone, and nitrogen oxides during urban smoke events in the western US. *Environ. Sci. Technol.*, **53**, 12 519–12 528, https://doi.org/10.1021/acs.est.9b05241.

Childs, M. L., and Coauthors, 2022: Daily local-level estimates of ambient wildfire smoke PM2.5 for the contiguous US. *Environ. Sci. Technol.*, **56**, 13 607–13 621, https://doi.org/10.1021/acs.est.2c02934.

Clements, C. B., N. P. Lareau, D. E. Kingsmill, C. L. Bowers, C. P. Camacho, R. Bagley, and B. Davis, 2018: The rapid deployments to wildfires experiment (RaDFIRE): Observations from the fire zone. *Bull. Amer. Meteor. Soc.*, **99**, 2539–2559, https://doi.org/10.1175/BAMS-D-17-0230.1.

Curtis, P. G., C. M. Slay, N. L. Harris, A. Tyukavina, and M. C. Hansen, 2018: Classifying drivers of global forest loss. *Science*, **361**, 1108–1111, https://doi.org/10.1126/science.aau3445.

Ding, K., and Coauthors, 2021: Aerosol-boundary-layer-monsoon interactions amplify semi-direct effect of biomass smoke on low cloud formation in Southeast Asia. *Nat. Commun.*, **12**, 6416, https://doi.org/10.1038/s41467-021-26728-4.

Fann, N., B. Alman, R. A. Broome, G. G. Morgan, F. H. Johnston, G. Pouliot, and A. G. Rappold, 2018: The health impacts and economic value of wildland fire episodes in the US: 2008–2012. *Sci. Total Environ.*, **610**, 802–809, https://doi.org/10.1016/j.scitotenv.2017.08.024.

Gong, X., A. Kaulfus, U. Nair, and D. A. Jaffe, 2017: Quantifying O_3 impacts in urban areas due to wildfires using a generalized additive model. *Environ. Sci. Technol.*, **51**, 13 216–13 223, https://doi.org/10.1021/acs.est.7b03130.

Huang, X., and Coauthors, 2023: Smoke-weather interaction affects extreme wildfires in diverse coastal regions. *Science*, **379**, 457–461, https://doi.org/10.1126/science.add9843.

Jones, M. W., and Coauthors, 2022: Global and regional trends and drivers of fire under climate change. *Rev. Geophys.*, **60**, e2020RG000726, https://doi.org/10.1029/2020RG000726.

Junghenn Noyes, K. T., and R. A. Kahn, 2023: Satellite multi-angle observations of wildfire smoke plumes during the CalFiDE field campaign: Aerosol plume heights, particle property evolution, and aging timescales. *J. Geophys. Res. Atmos.*, **129**, e2023JD039041, https://doi.org/10.1029/2023JD039041.

Kahn, R. A., 2020: A global perspective on wildfires. *Eos*, **101**, https://doi.org/10.1029/2020EO138260.

Kalashnikov, D. A., L. Schnell Jordan, T. Abatzoglou John, L. Swain Daniel, and D. Singh, 2022: Increasing co-occurrence of fine particulate matter and ground-level ozone extremes in the western United States. *Sci. Adv.*, **8**, 9386, https://doi.org/10.1126/sciadv.abi9386.

Kochanski, A. K., M. A. Jenkins, K. Yedinak, J. Mandel, J. Beezley, and B. Lamb, 2015: Toward an integrated system for fire, smoke and air quality simulations. *Int. J. Wildland Fire*, **25**, 534–546, https://doi.org/10.1071/WF14074.

——, D. V. Mallia, M. G. Fearon, J. Mandel, A. H. Souri, and T. Brown, 2019: Modeling wildfire smoke feedback mechanisms using a coupled fire-atmosphere model with a radiatively active aerosol scheme. *J. Geophys. Res. Atmos.*, **124**, 9099–9116, https://doi.org/10.1029/2019JD030558.

——, K. Clough, A. Farguell, D. V. Mallia, J. Mandel, and K. Hilburn, 2023: Analysis of methods for assimilating fire perimeters into a coupled fire-atmosphere model. *Front. For. Global Change*, **6**, 1203578, https://doi.org/10.3389/ffgc.2023.1203578.

Langford, A. O., and Coauthors, 2023: Were wildfires responsible for the unusually high surface ozone in Colorado during 2021? *J. Geophys. Res. Atmos.*, **128**, e2022JD037700, https://doi.org/10.1029/2022JD037700.

Lareau, N. P., and C. B. Clements, 2017: The mean and turbulent properties of a wildfire convective plume. *J. Appl. Meteor. Climatol.*, **56**, 2289–2299, https://doi.org/10.1175/JAMC-D-16-0384.1.

Mandel, J., J. D. Beezley, and A. K. Kochanski, 2011: Coupled atmosphere-wildland fire modeling with WRF 3.3 and SFIRE 2011. *Geosci. Model Dev.*, **4**, 591–610, https://doi.org/10.5194/gmd-4-591-2011.

——, M. Vejmelka, A. Kochanski, A. Farguell, J. Haley, D. Mallia, and K. Hilburn, 2019: An interactive data-driven HPC system for forecasting weather, wildland fire, and smoke. *2019 IEEE/ACM HPC for Urgent Decision Making (UrgentHPC)*, Denver, CO, IEEE, https://doi.org/10.1109/UrgentHPC49580.2019.00010.

National Interagency Fire Center, 2023: National Interagency Fire Center Open Data Site. Accessed 26 June 2023, https://data-nifc.opendata.arcgis.com.

Pausas, J. G., and J. E. Keeley, 2019: Wildfires as an ecosystem service. *Front. Ecol. Environ.*, **17**, 289–295, https://doi.org/10.1002/fee.2044.

Peng, Q., and Coauthors, 2021: Observations and modeling of NOx photochemistry and fate in fresh wildfire plumes. *ACS Earth Space Chem.*, **5**, 2652–2667, https://doi.org/10.1021/acsearthspacechem.1c00086.

Peterson, D. A., J. R. Campbell, E. J. Hyer, M. D. Fromm, G. P. Kablick III, J. H. Cossuth, and M. T. DeLand, 2018: Wildfire-driven thunderstorms cause a volcano-like stratospheric injection of smoke. *npj Climate Atmos. Sci.*, **1**, 30, https://doi.org/10.1038/s41612-018-0039-3.

——, and Coauthors, 2022: Measurements from inside a thunderstorm driven by wildfire: The 2019 FIREX-AQ field experiment. *Bull. Amer. Meteor. Soc.*, **103**, E2140–E2167, https://doi.org/10.1175/BAMS-D-21-0049.1.

Potter, B. E., 2012a: Atmospheric interactions with wildland fire behaviour–I. Basic surface interactions, vertical profiles and synoptic structures. *Int. J. Wildland Fire*, **21**, 779–801, https://doi.org/10.1071/WF11128.

——, 2012b: Atmospheric interactions with wildland fire behaviour–II. Plume and vortex dynamics. *Int. J. Wildland Fire*, **21**, 802–817, https://doi.org/10.1071/WF11129.

Prichard, S., and Coauthors, 2019: The Fire and Smoke Model Evaluation Experiment—A plan for integrated, large fire–atmosphere field campaigns. *Atmosphere*, **10**, 66, https://doi.org/10.3390/atmos10020066.

Rickly, P. S., and Coauthors, 2023: Influence of wildfire on urban ozone: An observationally constrained box modeling study at a site in the Colorado Front Range. *Environ. Sci. Technol.*, **57**, 1257–1267, https://doi.org/10.1021/acs.est.2c06157.

Roberts, J. M., and Coauthors, 2020: The nitrogen budget of laboratory-simulated western US wildfires during the FIREX 2016 Fire Lab study. *Atmos. Chem. Phys.*, **20**, 8807–8826, https://doi.org/10.5194/acp-20-8807-2020.

Robinson, M. A., and Coauthors, 2021: Variability and time of day dependence of ozone photochemistry in western wildfire plumes. *Environ. Sci. Technol.*, **55**, 10 280–10 290, https://doi.org/10.1021/acs.est.1c01963.

Rodriguez, B., N. P. Lareau, D. E. Kingsmill, and C. B. Clements, 2020: Extreme pyroconvective updrafts during a megafire. *Geophys. Res. Lett.*, **47**, e2020GL089001, https://doi.org/10.1029/2020GL089001.

Sarangi, C., Y. Qian, L. R. Leung, Y. Zhang, Y. Zou, and Y. Wang, 2023: Projected increases in wildfires may challenge regulatory curtailment of PM2.5 over the eastern US by 2050. *Atmos. Chem. Phys.*, **23**, 1769–1783, https://doi.org/10.5194/acp-23-1769-2023.

Schroeder, P., W. A. Brewer, A. Choukulkar, A. Weickmann, M. Zucker, M. W. Holloway, and S. Sandberg, 2020: A compact, flexible, and robust micropulsed Doppler lidar. *J. Atmos. Oceanic Technol.*, **37**, 1387–1402, https://doi.org/10.1175/JTECH-D-19-0142.1.

Sekimoto, K., and Coauthors, 2018: High-and low-temperature pyrolysis profiles describe volatile organic compound emissions from western US wildfire fuels. *Atmos. Chem. Phys.*, **18**, 9263–9281, https://doi.org/10.5194/acp-18-9263-2018.

Stow, D., P. Riggan, G. Schag, W. Brewer, R. Tissell, J. Coen, and E. Storey, 2019: Assessing uncertainty and demonstrating potential for estimating fire rate of spread at landscape scales based on time sequential airborne thermal infrared imaging. *Int. J. Remote Sens.*, **40**, 4876–4897, https://doi.org/10.1080/01431161.2019.1574995.

Strobach, E. J., W. A. Brewer, C. J. Senff, S. Baidar, and B. McCarty, 2023: Isolating and investigating updrafts induced by wildland fires using an airborne Doppler lidar during FIREX-AQ. *J. Geophys. Res. Atmos.*, **128**, e2023JD038809, https://doi.org/10.1029/2023JD038809.

Trainer, M., and Coauthors, 1993: Correlation of ozone with No_y in photochemically aged air. *J. Geophys. Res.*, **98**, 2917–2925, https://doi.org/10.1029/92JD01910.

U.S. Geological Survey, 2016: 1-meter GSD NAIP ortho imagery. Accessed 21 June 2023, https://doi.org/10.5066/F7QN651G.

Val Martin, M., R. A. Kahn, and M. Tosca, 2018: A global climatology of wildfire smoke injection height derived from space-based multi-angle imaging. *Remote Sens.*, **10**, 1609, https://doi.org/10.3390/rs10101609.

Wang, D., and Coauthors, 2021: Economic footprint of California wildfires in 2018. *Nat. Sustainability*, **4**, 252–260, https://doi.org/10.1038/s41893-020-00646-7.

Xu, L., and Coauthors, 2021: Ozone chemistry in western US wildfire plumes. *Sci. Adv.*, **7**, eabl3648, https://doi.org/10.1126/sciadv.abl3648.

Yokelson, R. J., and Coauthors, 2013: Coupling field and laboratory measurements to estimate the emission factors of identified and unidentified trace gases for prescribed fires. *Atmos. Chem. Phys.*, **13**, 89–116, https://doi.org/10.5194/acp-13-89-2013.